Open access • Journal Article • DOI:10.1016/0168-9002(96)00480-9

WA92: A fixed target experiment to trigger on and identify beauty particle decays

M. I. Adamovich, M. Adinolfi, Yu. Alexandrov, C. Angelini ...+67 more authors

Institutions: Lebedev Physical Institute, University of Genoa, University of Pisa, CERN ...+5 more institutions

Published on: 11 Sep 1996 - Nuclear Instruments & Methods in Physics Research Section A-accelerators Spectrometers Detectors and Associated Equipment (North-Holland)

Topics: Tracking (particle physics), Large Hadron Collider, Spectrometer, Charged particle and Lepton

EUROPEAN ORGANIZATION FOR NUCLEAR RESEARCH

CERN–PPE/96–66
15 May 1996

WA92: a fixed target experiment to trigger on and identify Beauty particle decays

The BEATRICE Collaboration

M. Adamovich[6], M. Adinolfi[3], Y. Alexandrov[6], C. Angelini[7], F. Antinori[2], C. Bacci[10], G. Barber[5], D. Barberis[3], D. Barney[5], J. Batten[5], W. Beusch[2], C. Bruschini[3], R. Cardarelli[9], A. Cardini[7], V. Casanova[3], F. Ceradini[10], G. Ciapetti[8], M. Dameri[3], G. Darbo[3], A. Di Ciaccio[9], A. Duane[5], J. P. Dufey[2], P. Farthouat[2], V. Flaminio[7], A. Forino[1], B. R. French[2], A. Frenkel[8], C. Gemme[3], R. Gessaroli[1], K. Harrison[1], N. Hummadi[5], R. Hurst[3], A. Kirk[2], F. Lacava[8], J. C. Lassalle[2], C. Lazzeroni[7], L. Malferrari[1], S. Maljukov[4], G. Martellotti[8], P. Martinengo[3], P. Mazzanti[1], J. G. McEwen[11], I. Minashvili[4], P. Musico[3], P. Nechaeva[6], A. Nisati[8], D. Orestano[10], B. Osculati[3], M. Passaseo[2], G. Penso[8], E. Petrolo[8], L. Pontecorvo[8], A. Quareni[1], H. Rotscheidt[2], V. Ryzhov[2], C. Roda[7], L. Rossi[3], N. Russakovich[4], C. Salvo[3], R. Santonico[9], G. Schuler[2], A. Semenov[4], A. Solovjev[4], M. Torelli[8], S. Veneziano[8], F. Vernocchi[3],M. Verzocchi[8], D. Websdale[5], M. Weymann[2], L. Zanello[8] and M. Zavertyaev[6].

Abstract

We describe the detectors and trigger system used in the CERN WA92 experiment. The experiment was designed to study the production and decay of beauty particles from 350 GeV/c π^- interactions in copper and tungsten targets. Charged particle tracking is performed using the Omega spectrometer. Silicon microstrip detectors are used to provide precise tracking information in the region of the production and the decay of heavy-flavoured particles and to trigger on the resulting high impact parameter tracks. The precision of vertex reconstruction corresponds to $\pm 3.7\%$ of the mean B-decay proper lifetime. Lepton and high transverse momentum hadron signals are also used in the trigger, which accepts 23% of B-decays and rejects 98.4% of non-beauty interactions.

(Submitted to Nucl. Instr. and Meth.)

[1] Università di Bologna and INFN, Bologna, Italy.
[2] CERN, Geneva, Switzerland.
[3] Università di Genova and INFN, Genoa, Italy.
[4] JINR, Dubna, Russian Federation.
[5] Blackett Laboratory, Imperial College, London, United Kingdom.
[6] Lebedev Physical Institute, Moscow, Russian Federation.
[7] Università di Pisa and INFN, Pisa, Italy.
[8] Università di Roma "La Sapienza" and INFN, Rome, Italy.
[9] Università di Roma "Tor Vergata" and INFN, Rome, Italy.
[10] Università di Roma "Roma Tre" and INFN, Rome, Italy.
[11] University of Southampton, Southampton, United Kingdom.

1 Introduction

CERN experiment WA92 used a π^- beam of momentum 350 GeV/c interacting in a 2 mm thick copper or tungsten target, situated upstream of the OMEGA spectrometer. The aim was to collect a large sample of B-decays and use this (a) to measure the cross-section for the hadronic production of B particles and (b) to measure separately the lifetimes of the identified charged $B^{\pm}$ and neutral B^0 mesons.

At this energy (26 GeV in the centre of mass) the fraction of interactions resulting in B production is less than 10^{-6}. It was therefore necessary to devise a selective trigger to enrich the data sample in B-decays and to equip the spectrometer with detectors able to discriminate the events containing B-decays from the much larger sample of background interactions.

Three features of the B events are exploited in the trigger scheme.

- The lifetime of the B-mesons ($\sim 10^{-12}$ s) and the large Lorentz boost results in a mean flight path $\sim$ 6 mm. A customised processor was designed to trigger on events compatible with such decay lengths using the signals from charged particles traversing a silicon microstrip vertex detector.
- A large fraction ($\sim$ 60%) of B-production results in a muon or an electron in the final state. An iron filter and an electromagnetic calorimeter were used to identify these leptons and to provide a component of the trigger.
- The high mass ($\sim$ 5 GeV/c^2) of the B-particles favours decay products with high transverse momenta. The magnetic bending of charged tracks is exploited at the trigger level to select events containing these high-p_T particles.

The ability to distinguish triggered events containing B-decays from the background events was enhanced by a compact high-precision silicon decay detector, which tracked the particles over the region where the decays occur and provided a precise, pictorial representation of the event topology.

In section 2 we present an overview of the WA92 experimental layout, followed by detailed sections (3—6) on the silicon detectors, the gas tracking detectors, electromagnetic calorimeter and muon filter. The trigger scheme, the data acquisition (DAQ) and the off-line analysis are described in sections (7—9). Comparison with Monte Carlo simulations are presented in section 10. Finally, the overall performance of the detectors, in terms of ability to identify short-lived heavy-flavour decays in the presence of a large background, is reviewed in section 11.

Data were collected in two runs, during 1992 and 1993. Improvements to detectors and triggers were implemented following the 1992 run. Some of the results reported here were obtained from an analysis of the 1992 data and this is specified, when relevant. Otherwise, all results refer to the 1993 run conditions.

2 Overview of the WA92 Experiment

2.1 The Omega Spectrometer

Omega (Ω) is a general purpose spectrometer [1], built at CERN in 1973 and used continuously in the SPS West Area where it has served many experiments. Each experiment has configured the Ω spectrometer according to its specific needs, retaining the magnet, the tracking chambers and the off-line reconstruction software, to which experiment dependent parts were added. WA92 has conformed to this model and this section briefly describes the configuration of the spectrometer used for the execution of the experiment.

The experiment layout is shown in Figure 1. The large superconducting Ω magnet provides a dipole field with bending power 7.2 Tm and a peak field of 1.8 T. This field is directed vertically, as indicated in Figure 1, and defines the z-axis of the reference system. The x-axis is defined by the incoming beam which is incident along the centre-line of the magnet. The origin of the reference system is at the target centre and the magnet centre is 350 cm downstream from the target.

2.2 The beam and experiment target

The H1 [1)] secondary beam from the CERN SPS was tuned to provide negative pions of momentum 350 GeV/c. Its properties are summarised in Table 1.

The experiment target was a metal disc, 2 mm thick with 5 mm radius: for the 1992 data taking period we used both Cu and W targets. The W target resulted in events with a higher multiplicity of interaction products and in 1993 only the Cu target was used.

2.3 Tracking detectors and lepton identification

Three silicon tracking devices are used. Upstream of the target, a silicon microstrip beam telescope is used to track the incident beam. Immediately downstream of the target is the Decay Detector, a high precision microstrip array in which the heavy-flavoured decays occur. This is followed by the Vertex Detector, again a microstrip array, equipped with fast read-out and used in the trigger. By placing the target and silicon detectors upstream and outside of the magnetic field the track

[1)] H1 is a CERN hadron beam reference code

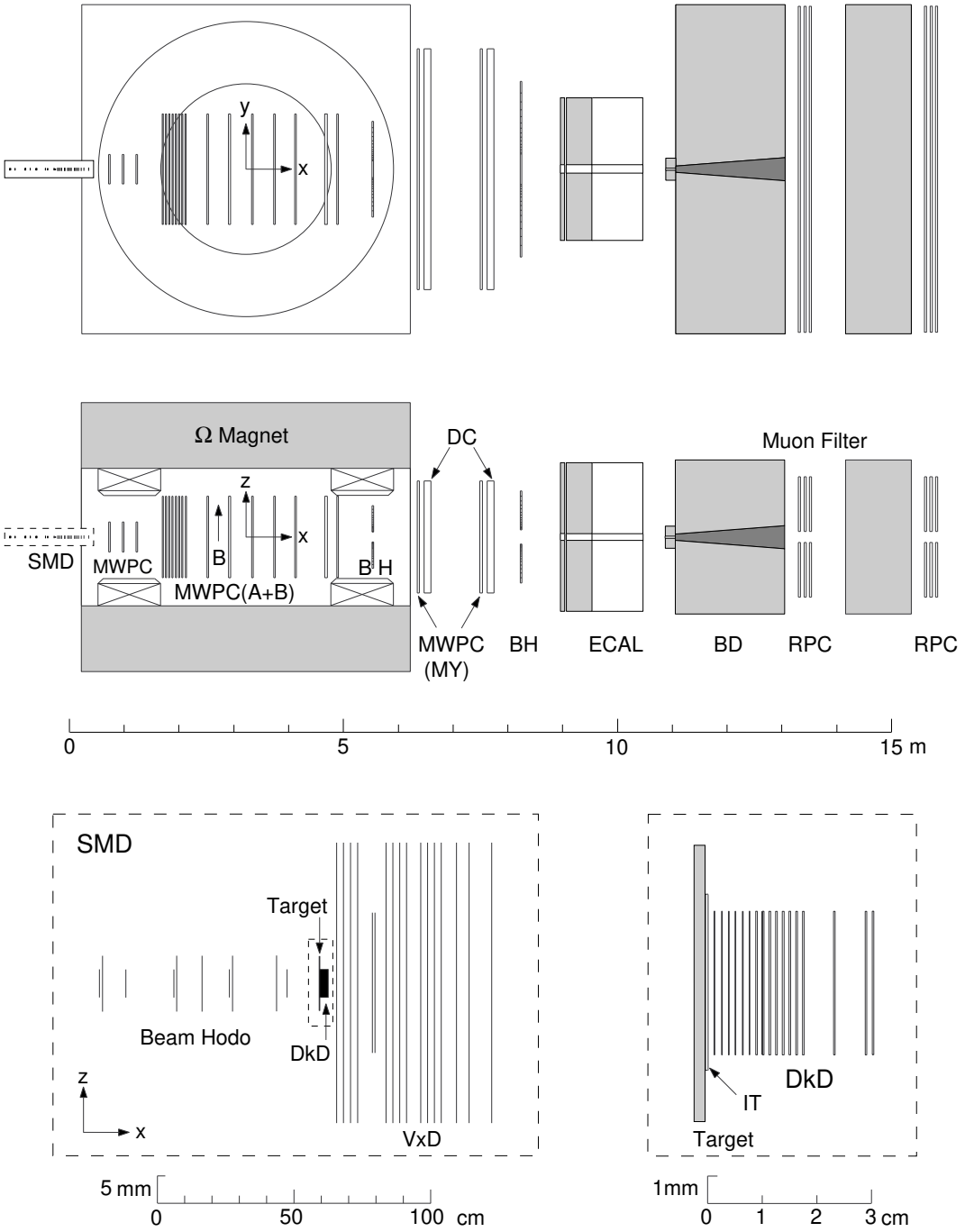

Figure 1: *Layout of the WA92 detectors and the Omega Spectrometer. Detector codes: BD–Beam Dump, BH–Bow-tie Hodoscopes, DC–Drift Chambers, DkD–Decay Detector, ECAL–Electromagnetic Calorimeter, IT–In-Target counter, MWPC–Multiwire Proportional Chambers, RPC–Resistive Plate Chambers, SMD–Silicon Microstrip Detectors, VxD–Vertex Detector.*

Momentum Momentum spread	$p = 350\,\mathrm{GeV}/c$ $\Delta p/p \sim 0.2\%$
Particles/spill on experiment target	5×10^6 π^- for 10^{13} p on the primary target
Spot size	2.2 mm FWHM
Divergence	1.4 mrad FWHM
K^-, $\bar{p}$ contamination	1.2%, 0.04%
spill length	2.4 s
period	14.4 s

Table 1: *Characteristics of the H1 beam*

recognition algorithm used in this trigger was simplified.

Three groups of Multiwire Proportional Chambers (MWPC) are situated within the Ω field volume and two large drift chambers track particles which leave the downstream exit of the magnet. The electromagnetic calorimeter, followed by an instrumented iron-wall muon filter, complete the downstream arm of the spectrometer. These detectors are described in more detail below.

3 Silicon Tracking Detectors

3.1 Beam telescope

The beam telescope comprises 10 planes of silicon microstrip detectors of 300 μm thickness. The active area is $5.12 \times 10.24\,\mathrm{mm}^2$ with 256 strips at 20 μm pitch. Five planes measure the y-coordinate and five planes measure the z-coordinate. The detectors are mounted on a marble optical bench, which also supports the decay and the vertex detectors.

3.2 Decay Detector

3.2.1 Structure of the decay detector

The Decay Detector (DkD) has been designed to detect and identify the B decays which occur within its volume. It consists of seventeen 10 μm pitch silicon microstrip planes occupying the region 3.2 cm downstream of the target (see Fig. 2). Each plane covers an area of $5 \times 5\,\mathrm{mm}^2$. The first microstrip detector was placed 1.7 mm downstream of the target, corresponding to about 1/3 of the average decay length of beauty particles produced by the 350 GeV π^- beam. The strips were oriented along the y-axis, yielding a measurement of the z-coordinate. This plane was followed by eleven (twelve in the 1992 run) additional microstrip planes, spaced by 1.2 mm in x, all with the same orientation as the first, to allow track reconstruction in the x-z projection (detectors oriented thus will be referred to as Z-planes). The array was completed by three planes (two in the 1992 run) measuring the y-coordinate and by two inclined planes used for projection matching. The spacing of the Y-planes and of the inclined planes was 5 mm. Each of the seventeen planes had 512 channels. A total of 8704 channels were thus packed in a volume of about $0.8\,\mathrm{cm}^3$.

The microstrip detectors were manufactured in two thicknesses, 150 μm and 300 μm. To minimize secondary interactions and multiple scattering and to optimize the two-track resolution in the region closest to the target, 150 μm thick detectors, each corresponding to 2.2×10^{-4} pion-interaction lengths and 1.6×10^{-3} radiation lengths, were used for the first six microstrip planes. The 300 μm thick detectors were used for the remaining eleven planes. They provide a higher detection efficiency and improved spatial precision.

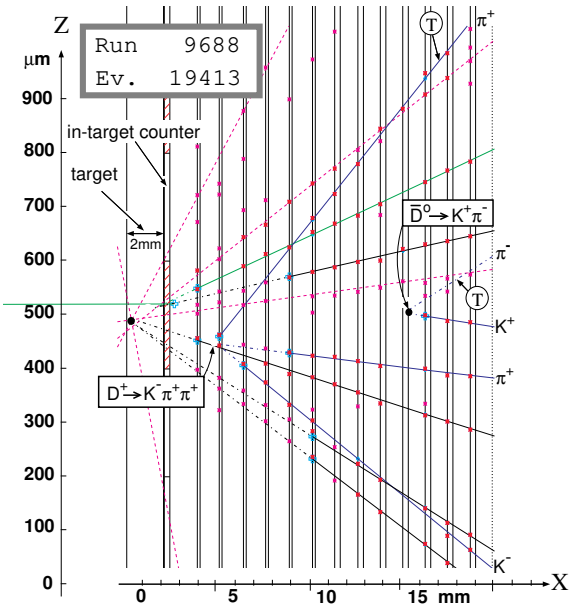

Figure 2: *Layout of the DkD for the 1992 experiment configuration. The display is a "double charm" event; the high spatial resolution of the DkD allows unambiguous identification of the primary and of the two charm-decay vertices. The tracks having an impact parameter larger than 100 μm (labelled by a T) triggered the impact parameter processor (BCP), described in section 7.7.*

Each microstrip detector plane is fabricated on a 14 mm$\times$14 mm silicon chip. This chip also carries the first stage of fan-out, consisting of metallised strips on the silicon dioxide. The chips are mounted on 250 μm thick ceramics which serve both as mechanical support and second stage fan-out. The final stage of fan-out is achieved using Kapton foil printed circuits which connect to the front-end electronics. The detectors were mounted in a $10 \times 10 \times 4$ cm^3 box, made of the same ceramic material as was used for the fan-out structure to avoid problems that might arise from differences in thermal expansion. The ceramic box was in turn mounted inside a larger box $24 \times 24 \times 8$ cm^3, constructed mainly from fibreglass and brass which also contained the target. The front and rear windows of this box were made of 25 μm mylar foils, aluminized to shield the interior from light and from ambient electronic noise. During data taking helium gas was circulated in this box to reduce hadronic interactions occurring in the gaps between the silicon planes. More details on the construction of the DkD can be found in Ref. [2].

3.2.2 Readout of the Decay Detector

Microstrip planes in the DkD were connected via the fan-out structure to four printed-circuit cards carrying the analogue front-end electronics. A front-end circuit card holds 8 daisy-chained Amplex [3] chips with 16 channels per chip. Each channel comprises a charge amplifier followed by a shaping amplifier and a track-and-hold stage. The peaking time of the shaper was about 500 ns. When an event trigger (Level-1) occurs, a strobe is sent to the track-and-hold stage which causes the signal amplitude to be stored until a reset is issued. This scheme allows read-out of the signal at the Level-1 trigger of the experiment, thus decreasing the dead time. The relatively long shaping time results in a long memory and out-of-time beam tracks are observed in the DkD. These were however invisible in the other detectors, which have a much shorter memory time.

The charge signals held by the Amplex were read out serially by CAMAC encoding modules (DRAMS [4]) which digitize the pulse heights with 8-bit precision and perform, separately for each channel, pedestal subtraction and suppression of signals below a preset threshold. Individual thresholds were computed twice weekly during data-taking as the sum of the pedestal mean value plus four times the standard deviation of the pedestal distribution.

3.2.3 Performance of the Decay Detector

Prior to its use in the experiment the detector's performance was investigated using a test beam [2]. Based on this experience the bias voltage was chosen to be 45 V for the 150 μm and 90 V for the 300 μm planes. These operating voltages gave a satisfactory signal-to-noise ratio and excellent efficiencies, as shown below.

The spatial precision and the hit efficiency were monitored during data taking. Non-interacting beam tracks and tracks emerging from interactions were used. In both cases the starting point was the reconstruction of clusters from individual strip hits. A cluster was defined to include an isolated hit or adjacent hits with no intervening pulse-height minimum. The position of each cluster was calculated as the centre of gravity of the hits which compose the cluster, weighted by their pulse heights. The spatial precision was evaluated using beam triggers. Beam tracks were first found in the silicon beam telescope and then extrapolated to the DkD. Clusters reconstructed in the Z-planes of this detector, in the extrapolation zone, were then fitted to straight lines. In the fit, all planes were used except the one whose precision had to be determined. Plots were then made of the distance between the intercept of the line with the given plane and the nearest cluster on that plane.

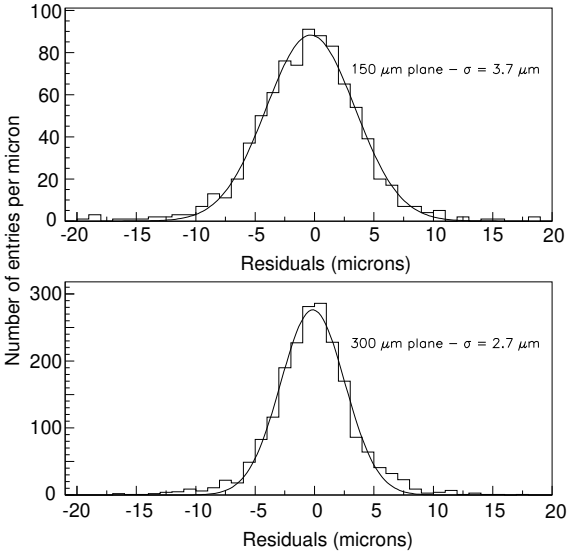

Figure 3: *Distribution of the residuals: (a) in the 150μm and (b) in the 300μm thick planes of the Decay Detector.*

Figure 3 shows the distributions obtained for the 150 μm planes and for the 300 μm planes. Fitting these distributions to gaussians we have obtained $\sigma = 3.7 \pm 0.2\,\mu$m for the 150 μm planes and $\sigma = 2.7 \pm 0.2\,\mu$m for the 300 μm planes. These results are consistent with the fact that in the 150 μm thick planes most clusters are contained within a single strip, whereas in the 300 μm thick planes the charge deposited experiences more lateral diffusion and clusters are typically two strips wide. The uncertainty in the cluster position was found to be consistent with the value of $10\,\mu\text{m}/\sqrt{12} \cdot \sqrt{\sum p_i^2}/\sum p_i$ where p_i is the pulse-height of the ith hit. The thin planes do however provide better two-track resolution, which was measured as $\sim 20\,\mu$m(25 μm) for the 150 μm(300 μm) planes.

The Decay Detector improves the spatial precision in longitudinal vertex position (x-coordinate) beyond what is obtainable using the other tracking detectors. For a quantitative evaluation of this improvement we have selected a sample of secondary interactions occurring in the DkD planes. This selection was based on a large energy deposition (see Sect.3.2.4 for details) and a minimum of three outgoing tracks. Figure 4(a) shows the resulting x-distribution of vertex position in the region of the seventh DkD plane while Figure 4(b) shows the corresponding distribution for vertices occurring in the region of the last Z-plane of the DkD (both planes are 300 μm thick). Fitting gaussians to these distributions one finds a sigma of 180 μm in the former case and 242 μm in the latter. After subtracting the contribution due to the finite plane thickness ($300/\sqrt{12} = 86.6\,\mu$m) we find that the precision in the longitudinal coordinate has improved by a fac-

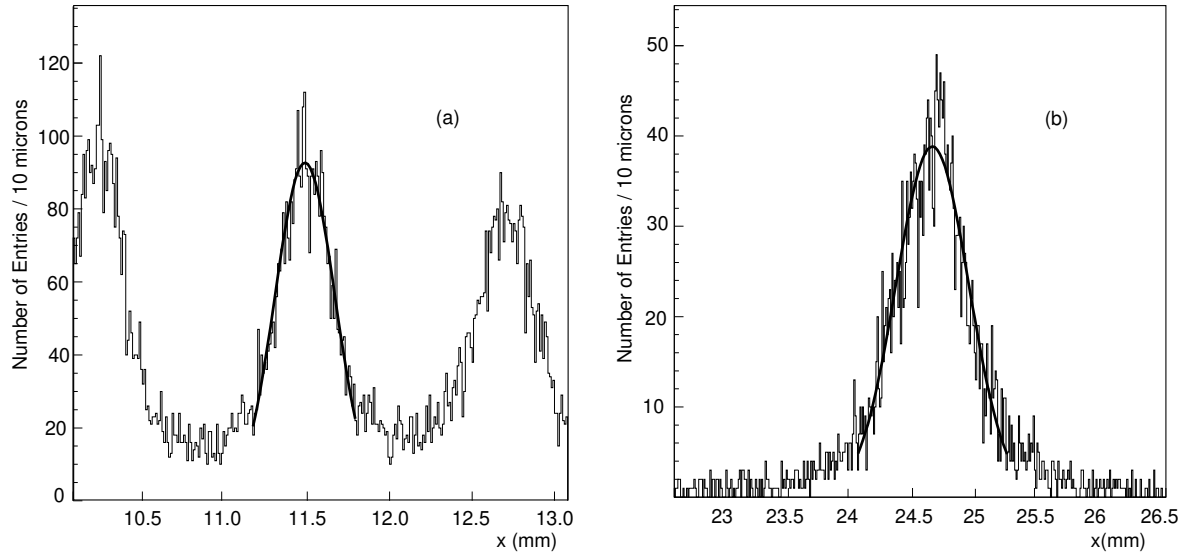

Figure 4: *Distribution of the longitudinal vertex coordinate: (a) using hits from the DkD, (b) when no information from the DkD is used in the reconstruction.*

tor of 1.4 due to the use of the hits provided by the six downstream Z-planes of the DkD.

Efficiencies were evaluated, using beam triggers, as the fraction of events in which a cluster was present in a microstrip plane within 10 μm of the predicted position. As in the measurement of the spatial precision, the prediction was based on track parameters, determined using all detectors except the one under consideration. The average efficiencies thus obtained, 91% for the 150 μm and 98% for the 300 μm planes, were checked using interaction triggers and found to be in excellent agreement.

The signal-to-noise ratio was also studied, using both beam and interaction triggers. There are two sources of noise hits: electronic noise and event-associated noise. The former contribution is found to be negligible. The latter arises mainly from δ rays and from cross-talk between channels. It has been studied as a function of distance from the reconstructed track and two components were identified. A uniform component, which contributes a number of clusters equivalent to 10% of the signal for the 150 μm and to 20% for the 300 μm planes. The second component is local to the track. It may be described as a tail of a track-centred gaussian distribution, having σ=18 μm , which starts 15 μm distant from the track. It amounts (in number of clusters) to 4% of the signal for the 150 μm and to 10% for the 300 μm planes.

3.2.4 Rejection of secondary interactions in the DkD planes

The DkD material corresponds in total to 0.6% of a π interaction length and to 4.5% of a radiation length. Photon conversions cannot mimic a decay vertex, since the e^+ e^- pair is reconstructed as a single track. Secondary hadronic interactions are however a major source of background. Their rate in minimum-bias events is expected to be $\sim 10^5$ higher than the signal due to B-decays. Figure 5 shows the x-distribution of reconstructed secondary vertices. The positions of the DkD planes where the secondary interactions occur are clearly visible.

A simple cut on vertex position cannot be used (without unacceptable loss of acceptance) to eliminate such interactions because of the small spacing between the DkD planes. However the fact that most hadronic interactions result in a large energy deposit in the silicon allows the analogue read-out to be used to advantage. A cut on the distance between the position of the reconstructed secondary vertex and the centroid of the largest energy deposit is found to reject about 91% of the vertices which are due to secondary interactions, while keeping 97% of Λ^0 and K^0_s decays and 92% of $D^0/D^\pm$ decays. The large background reduction is clear from the absence of structure in the distribution (see Fig. 5) of the vertices passing this cut and which are identified as K^0 decays.

3.3 Silicon Vertex Detector

The Vertex Detector (VxD) is a silicon microstrip array. It forms part of the WA92 tracking system and is also used to form the impact parameter trigger. Features pertinent to the former role are described here, those pertinent to the trigger are described in section 7.7.

3.3.1 Structure of the vertex detector

The VxD consists of 17 silicon-microstrip planes. There are 6 Z and 6 Y-planes, 3 W and 2 U-planes, which are tilted by 10.14° respectively to the Z and Y-planes. (The 1993 layout used an additional Y-plane and two planes at ±45°. Only one

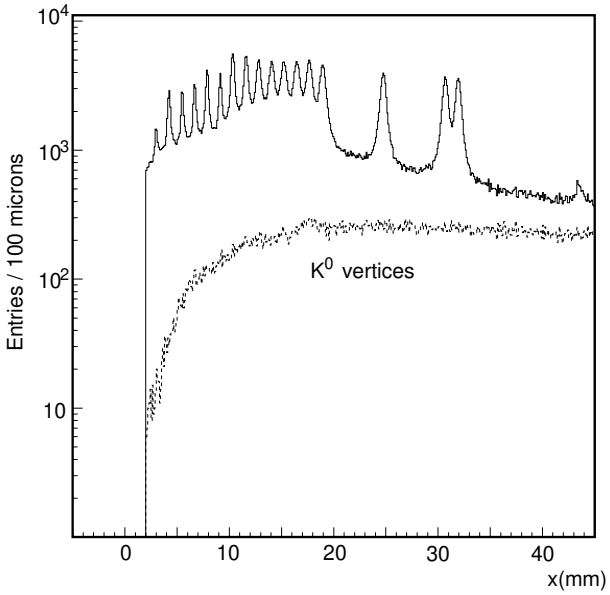

Figure 5: *Distribution of the secondary vertices in the Decay Detector region. Also shown (lower histogram) is the distribution of reconstructed vertices passing the pulse height cut and which are identified as K^0 decay vertices (their depletion at small decay lengths is an effect of the minimum impact parameter cut which is applied to tracks in the reconstruction of secondary vertices).*

Det. Plane	# planes	# strips per plane	pitch
Z_{Beam}	5	256/512	20 μm
Y_{Beam}	5	256/512	20 μm
Z_{VxD}	6	2048	25 μm
Y_{VxD}	6	2048	25 μm
$U^{(a)}_{VxD}$, $W^{(a)}_{VxD}$	3	1024	50 μm
$U^{(b)}_{VxD}$, $W^{(b)}_{VxD}$	2	512	50 μm

Table 2: *Characteristics of the microstrip detector planes for the beam telescope and for the VxD.*

W and one U-plane were used.) The main characteristics of these microstrip detector planes are summarized in Table 2, while the layout of the VxD with the same "double charm" event of Figure 2 is shown in Figure 6.

All the microstrip detectors have a thickness of 300 μm. Alternate channels are fanned out to opposite sides of the chip and are ultrasonically bonded, by 25 μm aluminium wires, to gold tracks laid out on a ceramic substrate. The square ceramics (either 300 μm or 600 μm thick), have a hole slightly smaller than the detector and serve both as a mechanical support and as first stage fanout. The gold tracks terminate on the four outer edges of the ceramic, up to 512 channels on each side, at a pitch of 250 μm. Kapton foils with overlaid gold tracks are glued to the edge of the ceramic and electrically connected with 25 μm aluminium wires, ultrasonically bonded. The kapton foils serve as the second stage of fanout. At the outer edge of these foils single-row pin connectors with an inter-pin pitch of 1.27 mm plug into the front-end cards.

3.3.2 Front-end and read-out architecture

Since the front-end, read-out and Beauty Contiguity Trigger (BCT) electronics [5]—[9] have already been reported in detail, we present here only a brief description.

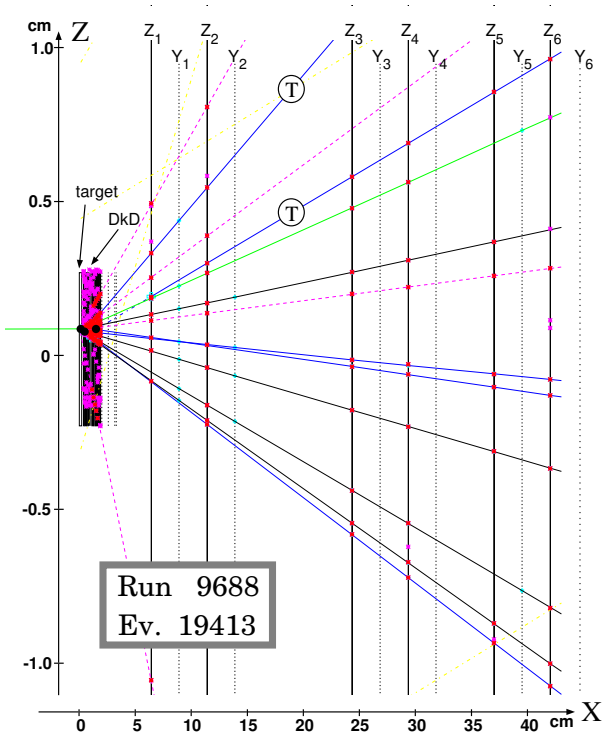

Figure 6: *Layout of the VxD. The 12 detector planes shown are the 6 Z_{VxD} (full line) and the 6 Y_{VxD} (dotted line), the 5 U_{VxD} and W_{VxD} which are not shown occupy the gaps Y_2-Z_3 and following Y_6. The superimposed event is the same "double charm" as in Figure 2 (which shows the DkD). The two high impact-parameter tracks selected by the BCP are labelled T.*

The Vertex Detector and the beam hodoscope comprise in total 27 microstrip planes, of which 2 Z-planes in the beam telescope and the 6 Z and 6 Y-planes from the vertex detector are equipped with a fast read-out and encoding system.

The fast system is required by the Z-planes, whose signals are used in the trigger processor (BCP, see Sect. 7.7). The processing time of the BCP is 35 μs so we designed a front-end system able to read, encode and transmit to the BCP all 13 000 microstrip channels in about 10 μs. The front-end cards for all microstrip channels (13 000 Z and 12 000 Y-planes), following transmission of data to the BCP, are read out by fastbus modules (COROM — COordinate Read-Out Module) in 30 μs.

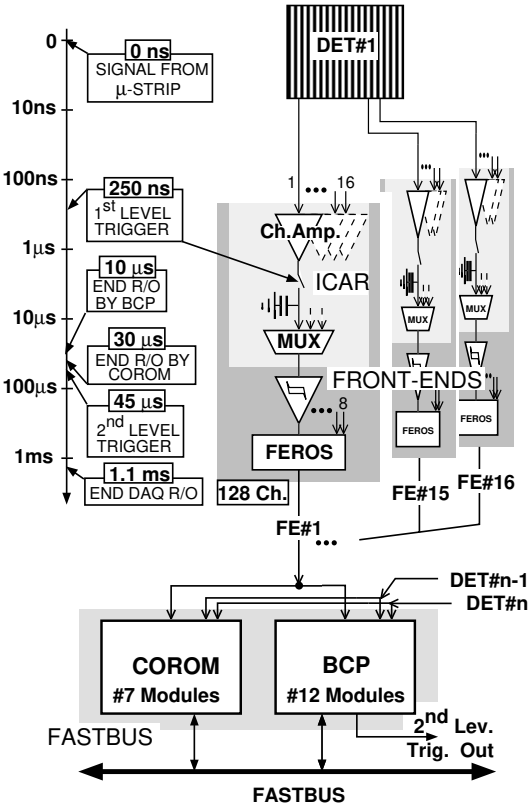

Figure 7: *Read-out and trigger architecture for the vertex detector. The time scale represents the sequence of actions involving the system from the signal coming out from the microstrips to the complete read-out of the event by Fastbus.*

The vertex detector was designed to work in a fixed target experiment; this requires an asynchronous system. The read-out operation starts with a Level-1 trigger that latches the peak values from the charge amplifier outputs (ICAR — Integrated Charge AmplifieR) and stores them in a capacitor. This trigger strobe must arrive within 250 ns following the interaction, corresponding to the propagation delay plus the peaking time in the ICAR amplifiers. The same strobe also starts the digitization of the microstrip hits by switching 16 capacitors (integrated in an ICAR) to the input of a discriminator and then encoding the addresses of the channels having a charge above a programmed threshold. A total of 128 channels, corresponding to 8 ICAR chips on a front-end board, is encoded by an ASIC chip (FEROS - Fast Encoding and ReadOut System).

The output from the FEROS chips, corresponding to the 16 front-end boards of one detector plane, are combined and transmitted through an interface, first to the BCP (only the Z-planes) and then to the COROM. In the event of a positive response from the second level trigger the seven COROM modules, which service the 14 detector planes are read out by fastbus in an average time of 1.1 ms. A block diagram of the system is shown in Figure 7.

3.3.3 Spatial precision

The VxD has no analogue read-out, so its spatial precision is determined by the 25 μm strip pitch. This is quite adequate for calculation of the impact parameter in the BCP trigger. However, the precision in vertex reconstruction is determined by the DkD, which contributes hits with much higher spatial precision, as was already seen in Figure 4.

4 MWPC and Drift Chambers

The arrangement of Multi-wire proportional chambers (MWPC) and drift chambers is shown in Figure 1. Inside the Ω magnetic field, there are 58 planes of MWPC. Going from upstream to downstream we encounter: 12 planes with 1 mm pitch (1MM chambers), 42 planes with 2 mm pitch (A and B chambers) and 4 planes with 4 mm pitch (MY chambers). Different orientations of the anode wires allow reconstruction of track trajectories in space. The 1MM chambers are placed at the entrance of the magnet and are used in matching the tracks found in the spectrometer with those found in the microstrip vertex detector; they have a sensitive area of $\sim 25 \times 25\,\mathrm{cm}^2$. The A and B chambers occupy the central region of the magnet and are used for pattern recognition and momentum measurement; they have a sensitive area of $\sim 150 \times 100\,\mathrm{cm}^2$. Finally, the MY chambers are placed following the exit of the magnet. They are used primarily to eliminate ambiguities in the drift chamber measurements and have a sensitive area of $\sim 310 \times 150\,\mathrm{cm}^2$. All the MWPCs use the same 40 MHz read-out system [12] which records the address of each channel above threshold. The accuracy in momentum measurement obtained with the MWPC system alone is: $\sigma_p/p^2 = 10^{-3}(\mathrm{GeV/c})^{-1}$.

Two sets of large drift chambers (DC1 and DC2), each with 4 planes covering an area of $\sim 320 \times 150\,\mathrm{cm}^2$, are placed immediately downstream of the magnet. The anode wires in these chambers are spaced 5 cm apart, and track coordinates are measured with an accuracy of $\sim$ 0.2 mm, yielding an improved momentum measurement ($\sigma_p/p^2 = 3 \times 10^{-4}\,(\mathrm{GeV/c})^{-1}$) for tracks which are not swept away by the magnetic field of Ω ($p > 5\,\mathrm{GeV/c}$).

5 Electromagnetic Calorimeter

5.1 Detector description

Electron identification and triggering have been performed using the OLGA [13] lead glass calorimeter. Its front face was situated a distance of 950 cm downstream from the target. The calorimeter is composed of three elements, as shown in Figure 8.

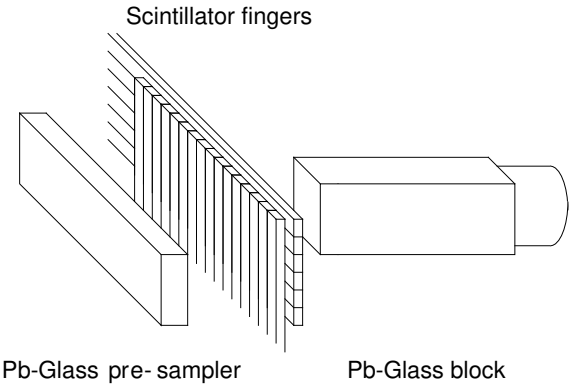

Figure 8: *Schematic layout of elements of the OLGA electromagnetic calorimeter.*

- An active presampler comprising two columns of 19 lead glass slabs (type F2W). Each slab is 145 cm long by 14 cm high and has a depth of 10 cm which corresponds to three radiation lengths. Electrons incident on the sampler will start to shower so the energy deposited in the sampler can be used to discriminate between pions and electrons.
- A shower position detector which consists of four half planes of scintillator fingers: two half planes of horizontal fingers and two half planes of vertical fingers. Each half plane contains 168 fingers, each finger being 152 cm long, 1.53 cm wide and 1 cm deep. The pulse height from each finger is used to determine the centre of a shower within ± 4 mm.
- An array of 18×19 lead glass blocks (type SF5) with surface $14 \times 14\,\mathrm{cm}^2$ and depth 47 cm, corresponding to 18.5 radiation lengths. A block at the centre was removed to allow the beam to pass through.

5.2 Calibration

The calibration of the calorimeter was performed in two steps. First, the muon chamber system was used to trigger on halo muons. The muons traversing the lead glass deposit 0.11 GeV in the sampler and 0.65 GeV in the lead glass blocks. Approximately 1000 muons incident on each lead glass block were used to perform this calibration. A second and more accurate calibration was performed using e^+e^- pairs, reconstructed in the spectrometer and tracked downstream to the calorimeter. The ratio of the energy of the showers, measured in the calorimeter, relative to the momentum of the tracks, as measured in the magnetic spectrometer, was used to calculate calibration factors for each block. Figure 9 shows the resulting E/p spectrum, integrated over the whole calorimeter, for electrons in high multiplicity events. The minimum momentum of these electrons is $8\,\mathrm{GeV}/c$ and their mean momentum is $17\,\mathrm{GeV}/c$.

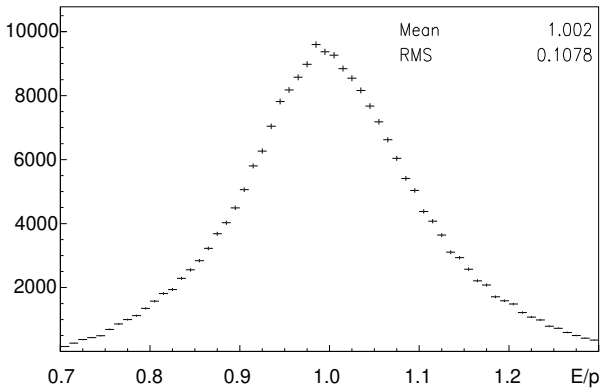

Figure 9: *Distribution of the ratio E/p, summed over all calorimeter cells.*

5.3 Energy and position resolution

The energy resolution of the calorimeter can be parameterized as

$$\frac{\sigma(E)}{E} = \frac{0.15}{\sqrt{E\,(\mathrm{GeV})}} \oplus 0.08\ .$$

In the central region several track impacts and showers may overlap. This region is not used in the trigger and was excluded in the above analysis.

The precision in the measurement of a shower's position is dependent on whether or not the finger information is present. When the finger information is present in a projection the positional accuracy is $\pm$ 4 mm. When the finger information is absent the shower position is calculated using the shower profile in the lead glass block. Two photons can be resolved fully if they are separated by more

than 20 cm. Below this separation the resolution depends on the energy of the two photons.

5.4 Electron identification

The electron identification criteria require an energy deposition greater than 1.5 GeV in the sampler and a finger cluster associated with the shower in at least one projection. In addition, the ratio of the energy of the associated electromagnetic shower to the charged particle momentum is required to be greater than 0.8. Cuts are imposed on the shower shape and isolation. These cuts are "loose" or "tight", depending on whether electron identification efficiency or hadron rejection power needs to be optimized. The electron identification efficiency in high multiplicity events increases from 24 (38)% at $p_{\rm T} = 0$ to 42 (60)% at $p_{\rm T} = 1.2\,{\rm GeV}/c$ for "tight" ("loose") cuts; the corresponding rejection factors for hadrons, measured using pions from $\rm K^0_s$ decays, are respectively $\times 100$ ($\times 15$), independent of $p_{\rm T}$.

6 The Muon Filter

6.1 Detector description

The muon trigger hodoscope has been described in detail elsewhere [16]. It consists of two identical detector planes. The first is situated downstream of a 2.0 m thick iron absorber and the second behind an additional 1.2 m thick iron absorber. The core of the first absorber is made from discs of tungsten which absorb the 350 GeV/c π^- beam. This beam-dump is 1.98 m long (about 21 interaction lengths (λ) and the discs have increasing radii to cover a cone of semi-vertex angle 25 mrad centred on the beam line. The thickness of the first absorber (about 12 λ) is chosen to filter out most of the hadrons produced in the target, while keeping the multiple coulomb scattering of high energy muons at a level which is sufficiently low to allow association of tracks measured in the hodoscope with those measured in the spectrometer. The presence of the second absorber (about 8 λ) ensures that only muons reach the second plane of the hodoscope.

There are two major background sources: muons that originate from decays in flight of pions and kaons which are produced in the target, and muons that originate in hadron showers initiated in the electromagnetic calorimeter (its thickness is $\sim 1\,\lambda$). This latter component has a softer momentum spectrum and a wider angular distribution. It is strongly reduced by requiring hits recorded in the hodoscope to be collinear with the target.

Particles with low transverse momenta are deflected horizontally in the field of the Ω magnet and remain close to the central plane. This region is thus populated mainly by decay muons that originate from parents emitted with low transverse momenta. For this reason, each hodoscope plane has been divided into two (upper and lower) halves. Each half hodoscope has an angular acceptance of $8 \leq |\theta_z| \leq 70$ mrad in the vertical projection and $|\theta_y| \leq 180$ mrad in the horizontal projection. The area covered by each hodoscope plane is 12 $\rm m^2$, the distance of the hodoscope planes from the target is 13.9 m and 16.0 m respectively.

The hodoscope is built from Resistive Plate Chambers, RPC [17]. Each hodoscope is made of three detector planes, two equipped with horizontal read-out strips (Z-chambers) and one with vertical read-out strips (Y-chamber). The Z-chambers are used to reconstruct the muon track in the non-bending projection. The Y-chambers improve the association with the tracks measured in the spectrometer. Each detector plane is made of 6 RPCs of dimensions $1 \times 2\,{\rm m}^2$, slightly overlapped in the y-direction to avoid dead regions. Two Z-chambers and one Y-chamber constitute a module and six of these modules, covering an area of 12 $\rm m^2$, are hung from a support frame prior to installation in the experiment.

The read-out electrodes of the RPC are segmented in strips of 31 mm pitch. The Z-chambers are equipped with read-out strips 2 m long and the Y-chambers with 64 read-out strips 1 m long. The width of the signals is 40 ns, thus ensuring that halo muons traversing the hodoscope have a small probability of accidental coincidence with the interaction trigger.

6.2 Muon selection

A simple algorithm is used in the off-line software to reconstruct the muon tracks. First, space points are reconstructed in the two hodoscopes using the hits in the two projections of the RPCs. Then the tracks reconstructed in the spectrometer are extrapolated to the two hodoscopes and matched with the space points. If no hit is present in one of the two projections of the hodoscope the centre of the chamber is used instead, with a cluster size equivalent to the size of the chamber module in the appropriate projection.

Figure 10 shows the scatter plot of the distance in the y and in the z-projections between the track extrapolation and the space points reconstructed in the first hodoscope. The peak at $\Delta y = \Delta z = 0$ corresponds to the correct association between a muon reconstructed in the spectrometer and the hits in the hodoscopes. The width of this peak is consistent with the detector resolution, the effect of multiple coulomb scattering and the kinematics of the decays in flight of pions and kaons produced in the target. The almost flat background is instead due to random association between the muon hits in the RPC and other tracks reconstructed in the spectrometer. As explained above, for those events in which the Y-chambers were inef-

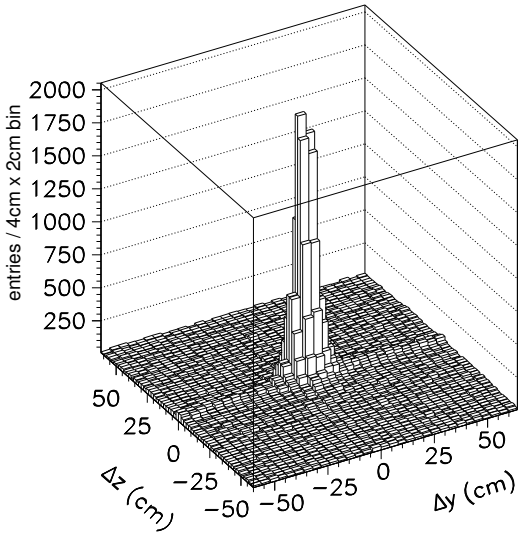

Figure 10: *Distribution of the distance (in the y-z plane) between the extrapolation of all the tracks in the spectrometer and the space points reconstructed on the first muon station.*

ficient, we used the centre of the chamber to reconstruct the space points: this explains the small enhancement at $\Delta z = 0$ over the whole y-range of each module which can be seen in the two-dimensional residual distribution.

A track reconstructed in the spectrometer is identified as a muon when it matches at least one space point in both hodoscopes. A tolerance (taking into account the cluster size of each space point) of three times the r.m.s of the peak shown in Figure 10 is permitted. The association probability, estimated using simulated events, is larger than 97% for muons with momenta above 10 GeV/c.

The background due to the association of the muon hits in the hodoscope with a "wrong" track reconstructed in the spectrometer is $(7.1 \pm 0.2)\%$: this value has been obtained from real data, mixing the tracks reconstructed in one event with the muon hits in the hodoscopes from another event. It is consistent with the background which can be observed below the peak of the distribution of Figure 10.

When the efficiency of the muon trigger (97%) is also taken into account, the overall detection efficiency for muons of momenta greater than 10 GeV/c is 94%.

7 The trigger system

7.1 Overview

The trigger system has been designed to fulfil the requirements of detector strobing, background rejection, and high beauty acceptance whilst maintaining reasonably low dead-time. High beauty acceptance has been achieved using the impact parameter trigger (BCT) in conjunction with muon, electromagnetic calorimeter (ECAL) and high p_T triggers. The elements of this trigger scheme are described in the following sections. The fast read-out electronics of the silicon detectors and the significant (35 μs) processing time of the BCP, impose stringent requirements on the trigger: a fast strobe (pre-trigger) must be provided within 250 ns of the interaction and the BCT must provide good rejection of background so as to reduce dead-time. A multi-level trigger has therefore been implemented. Figure 11 shows a schematic of the system where dead-time, rates and decision timings at the various stages are indicated.

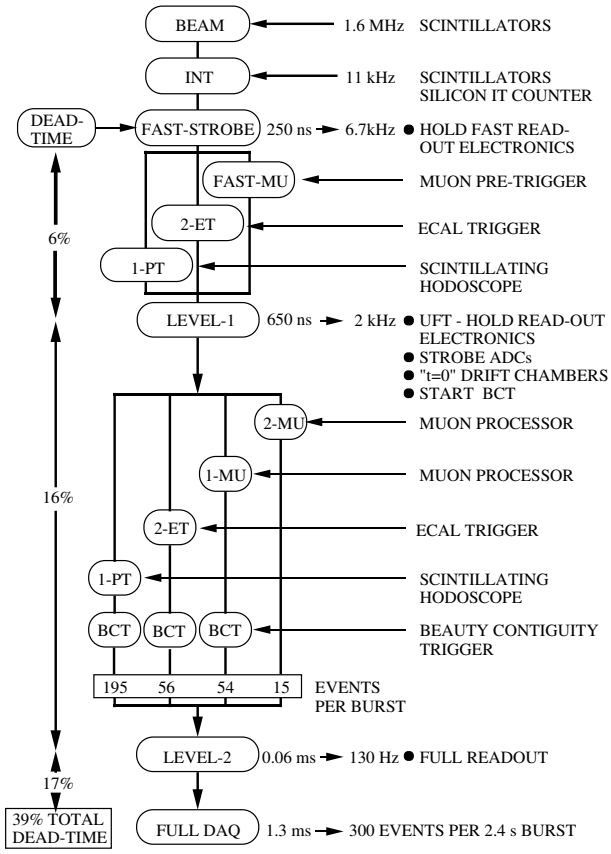

Figure 11: *Logical scheme of the WA92 trigger, with typical rates.*

The Level-1 trigger logic is built from NIM standard electronics, situated adjacent to the Ω magnet to reduce signal delays. The Level-2 trigger is located in the counting room.

7.2 Beam and Interaction trigger

The beam particles were identified by the coincidence of three scintillation counters $S_1 \cdot S_2 \cdot \overline{V}_1$, placed upstream of the target as shown in Figure 12: The veto counter V_1, 20 cm upstream of the target,

rejected beam halo particles at a distance between 2 and 30 mm from the beam axis in a time interval of ± 30 ns from the triggering beam particle.

Interactions were selected by the coincidence between the beam counters, two additional scintillators (S_3, S_4) placed downstream of the target and a silicon "in-target" counter (IT). The interaction trigger (INT) is thus defined: $\mathrm{INT} = S_1 \cdot S_2 \cdot \overline{V}_1 \cdot \mathrm{IT} \cdot S_3 \cdot S_4$. The two scintillators, S_3 and S_4, measured 10 cm in y and 6 cm in z. They were placed 72 cm downstream of the target, above and below the beam axis, with a gap of 2 cm. They were sensitive to single minimum ionizing particles and used to select inelastic interactions. The veto counter, V_2 ($2 \times 2\,\mathrm{cm}^2$), placed at the exit of the Ω magnet at a distance of 6.5 m from the target, was used to reject non-interacting beam particles in a time interval of ± 30 ns from the interaction.

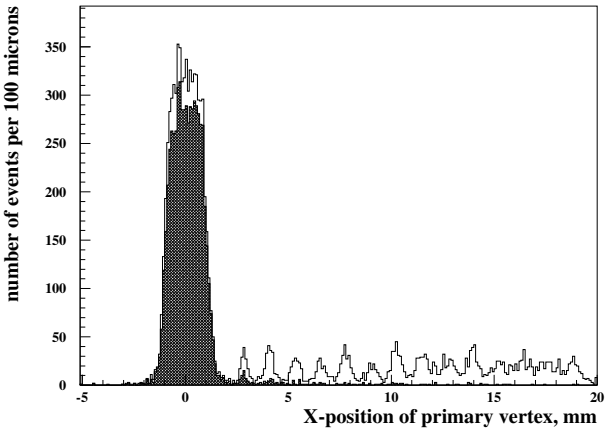

Figure 13: *Distribution of the x-position of primary vertices in events selected with the interaction trigger. The shaded region indicates those found in events triggered with the "in-target" counter.*

The IT counter was a 300 μm thick silicon detector glued to the downstream face of the target. It consisted of 22 strips with a pitch of 200 μm, measuring the z-coordinate. The signals from each strip were amplified and discriminated at the equivalent of a 500 keV energy deposit, corresponding to approximately five minimum-ionizing particles. This IT counter performed two functions. First, it enriched the sample with interactions in the target. Secondly, it confirmed the position of the primary interaction given by the beam telescope, an essential feature of the impact parameter trigger described below (Sect. 7.7). The effect of the IT is shown in Figure 13. It accepts 93% of primary interactions in the target which are selected by the coincidence between the beam trigger and the S_3 and S_4 scintillators. Without the IT counter $\sim 40\%$ of primary interactions occur downstream of the target; the fraction is reduced to 4% by including the IT counter in the coincidence. This results in an important reduction of Level-1 triggers due to interactions in the silicon detectors, which would provide a source of unwanted BCP triggers at Level-2.

7.3 The high-p_T trigger

Two planes of scintillator hodoscopes (HZ0 and HZ1 in Fig 14) were placed near the exit of the Ω magnet. An earlier version of these hodoscopes is described in [14].

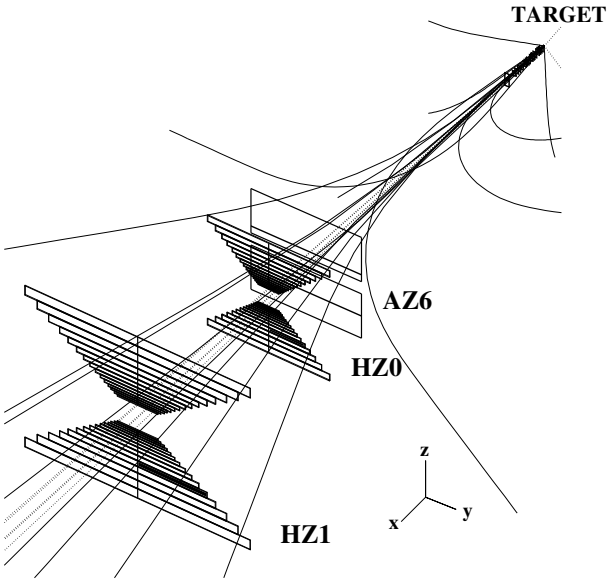

Figure 14: *Layout of the scintillator hodoscopes used in the high-p_T trigger.*

Particles with low transverse momenta are swept by the magnetic field in the horizontal plane, while particles of large transverse momentum are distributed over the plane perpendicular to the beam direction. The two scintillator hodoscopes, HZ0 and HZ1, are "bow-tie" shaped in order to be insensitive to particles with a transverse momentum smaller than 0.6 GeV/c and to accept the pseudorapidity region $3 < \eta < 6$. Each hodoscope has four quadrants of 15 slabs each, arranged in a projective geometry pointing to the target in the non-bending plane. The areas of the slabs were smaller for those nearer to the beam so that they had approximately equal counting rates for particles emerging from the target.

The transverse momentum trigger was derived from a simple coincidence of the corresponding slabs in the two planes of scintillators with the fast OR signals from groups of 8 wires ($\Delta z = 16$ mm) of one of the A chambers (AZ6) having horizontal wires. The coincidence between the slabs in the hodoscopes and the fast OR signal of the MWPC was made using purpose-built modules. The efficiency for triggering on tracks within the acceptance of the hodoscopes was 80%, and the trigger was available 300 ns after the interaction.

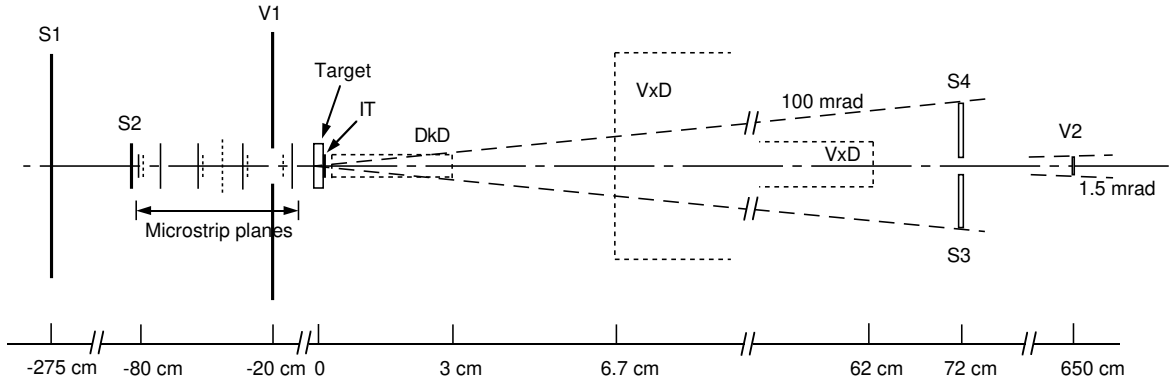

Figure 12: *Layout of the counters used for the beam and the interaction triggers.*

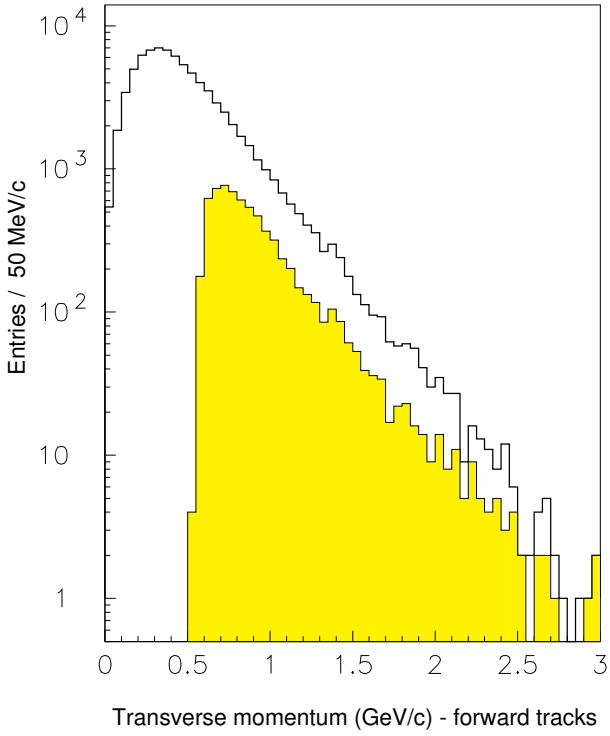

Figure 15: *Transverse momentum distribution for forward tracks reconstructed in the Ω spectrometer. Those tracks which satisfy the high p_T trigger condition are shaded.*

Figure 15 shows the transverse momentum spectrum for tracks reconstructed in the MWPCs and drift chambers. These tracks are produced at angles less than $\sim$ 100 mrad and have momenta $> 7\,\mathrm{GeV}/c$. The tracks which trigger are shown in the shaded region. More than 1/3 of the tracks which have $p_T > 0.75\,\mathrm{GeV}/c$ trigger. Requiring at least 1 (2) high-p_T concidence(s) in the event reduced the interaction rate by a factor 2.5 (8). The comparison with simulation is shown in Table 4.

7.4 The Muon trigger

The muon trigger uses signals from the RPC chambers in the muon filter (Sect. 6). It is formed in two stages. The muon pre-trigger is available at the same time as INT and is used to strobe the RPC read-out. The second stage uses a special processor, which provides the final muon trigger in time for Level-2.

7.4.1 Muon pre-trigger

Signals from the strips of each RPC are OR-ed together. The OR signals from all RPC Z-chambers form a prompt muon pre-trigger that is used, in coincidence with the interaction trigger, to send a fast strobe to the muon trigger processor and to the strip read-out modules. This pre-trigger was made by a fast logic circuit located close to the hodoscope. It formed a coincidence of three out of the four Z-planes of the hodoscope. The time jitter was a few nanoseconds, mainly due to the different propagation times of the signals along the strips. The efficiency of the "3 out of 4" pre-trigger was higher than 99%.

Besides the requirement for a fast response at the trigger level, good time resolution is also needed to avoid accidental coincidences of halo muons with the interaction trigger. The profile of the halo accompanying the beam is peaked in a small region around the beam. This is due to muons in the aperture of the beam transport magnets. But there

is also a large number of muons distributed almost uniformly over the surface of the hodoscope, amounting to about 1% of the pion beam intensity. With a typical beam intensity of 5×10^6 π/spill, the hodoscope rate due to the muon halo was about 6×10^4 counts/spill.

7.4.2 Muon trigger processor

The muon trigger processor is described in detail elsewhere [15]. It selects tracks pointing to the target in the non-bending plane. Since the RPC hodoscope is symmetric with respect to the central horizontal plane, two identical processors work in parallel. The inputs to the processor are the signals from the 768 strips of the RPC Z-chambers. The signals from the strips at a given z-coordinate in the same hodoscope are OR-ed together: this results in 64 OR-ed signals sent to each processor. To associate the hit pattern to the interaction vertex, the processor defines roads of programmable width and angle. These roads are mapped onto a 32×32 matrix made of 16 fast programmable logic devices with a 12 ns (typical) propagation time. The response is available after a fixed processing time of 90 ns. The efficiency of the muon trigger was measured to be $\sim$97% (the small loss is due to the time jitter of the signals).

Hits in the first hodoscope plane corresponding to patterns accepted by the trigger logic are loaded in a 32-bit register. The data from the two registers are used in a cluster-finding algorithm to define the multiplicity of tracks pointing to the target. During normal data taking the muon trigger processor selected coincidence patterns of one strip of the first hodoscope plane with any one of three strips of the second plane to provide an inclusive muon trigger (multiplicity ≥ 1) and a dimuon trigger (multiplicity ≥ 2).

To penetrate the iron filter and satisfy the target-pointing condition of the trigger processor, muons must have a momentum of at least 7 GeV/c. Due to the minimum angle accepted by the hodoscope, the muon trigger results in a transverse momentum cut of about 100 MeV/c. The rates of the inclusive muon trigger and of the dimuon trigger were, respectively 3×10^{-2} and 10^{-3} of the interaction trigger rate (see Table 4), in agreement with the expected number of pion and kaon decays in flight. The contribution resulting from hadron interactions in the calorimeter and the filter is strongly reduced by the pointing requirement of the trigger.

Figure 16 shows the longitudinal and transverse momentum distribution of tracks which are identified as muons compared with those of all tracks reconstructed in the spectrometer. Distributions of muon tracks selected by the dimuon trigger are also shown. All these distributions are well reproduced by Monte Carlo generated events with full simulation of the detector response.

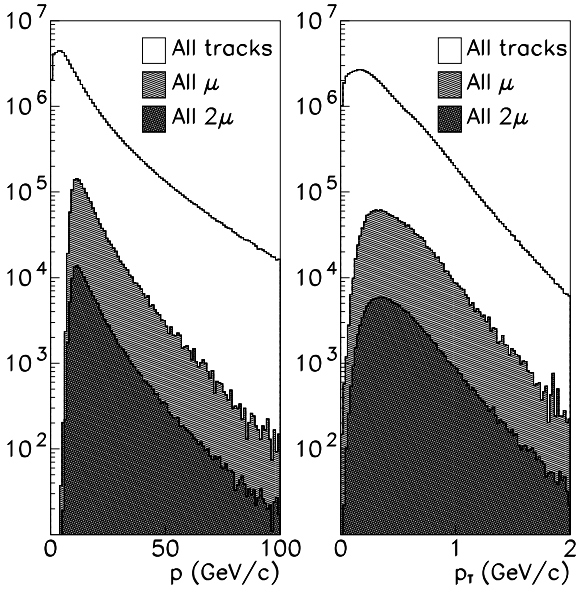

Figure 16: *(a) Longitudinal and (b) transverse momentum distributions for all charged tracks, for single muons and for muons in dimuon-triggered events.*

7.5 ECAL trigger

The OLGA calorimeter was used to trigger on high transverse electromagnetic energy. The central three rows of lead glass blocks suffered a high rate of charged hadron interactions and so were excluded from the trigger. A threshold energy deposition was calculated for each lead-glass block according to its position in the array and corresponding to a given $E_{\rm T}$ threshold.

The trigger required two or more blocks with $E_{\rm T} > 0.65$ GeV. A trigger rate of 2.6% of interaction triggers was obtained (see Table 4). The acceptance for beauty events was estimated from the Monte Carlo simulation to be 10%.

7.6 Level-1 trigger

The beam (BEAM) and interaction (INT) triggers are available 250 ns after the beam interacts in the target. The interaction trigger is sent to the fast read-out electronics of the VxD and beam silicon detectors, providing a "hold" signal to the ICAR chips. A "wait Level-1" starts, introducing a 5 μs dead-time due to the ICAR recovery period. Following INT, and before Level-1, multiple-beam events are filtered using scintillator S2 (upstream of the target) and V2, which detects (non-interacting) beam particles exiting the Ω magnet. This reduces the INT rate by 27%. The Level-1 trigger is defined at 650 ns using the high $p_{\rm T}$, the muon pre-trigger and ECAL triggers by forming the logical "OR" of their outputs. Level-1 provides the User Fast Trigger (UFT) in the standard Ω trigger logic [1] and

strobes all the detectors. The BCT trigger and the "wait Level-2" are also started, introducing a 60 μs dead-time.

7.7 Beauty Contiguity Processor

A topological trigger on secondary vertices is very effective in exploiting the long ($\sim 10^{-12}$ s) lifetime of beauty or charmed hadrons. The trigger on events with secondary vertices that we designed for WA92 [6]–[8] uses a parallel algorithm for track finding that is based on the concept of a "contiguity mask" [10], from which the name, Beauty Contiguity Processor (BCP), is derived. The trigger algorithm is divided into three sequential steps:

- First the primary interaction vertex is found by extrapolating the beam track (using hits from two of the five Z-planes of the beam silicon telescope) into the thin target. This step is executed by two FBCTs (FEROS to Beauty Contiguity Trigger interface). The selection of events with a primary vertex inside the target is improved using the correlation between the z-coordinate of the extrapolated beam and the z-coordinate given by the IT counter (described in Sect. 7.2). Since the IT counter is only 100 μm downstream of the target, its z information, allows a better definition of the primary vertex. By discarding downstream interactions and, in case of multiple beam crossings within the resolution time of the front-end electronics, by rejecting wrongly-selected beam tracks, two potential sources of wrong BCT triggers are reduced. The correlation between the beam tracks, as found by the FBCT and the IT counter, is executed by the BFPR (Beam Filter PRocessor) module. The improvement achieved by the BFPR is evident in Figure 17, which shows the reduction (by 60%) in the number of downstream-of-target primary interactions.
- Next, the primary tracks, i.e. tracks extrapolated back to within 100 μm of the previously-found main vertex, are found, counted and their hits erased from the event. The remaining hits are then used to reconstruct tracks with impact parameter between 100 μm and 1 mm from the primary vertex. The tracks are reconstructed in the x-z projection using 6 detector planes and the algorithm is executed by 8 BCPS modules (Beauty Contiguity Processor Slice). The 8 interconnected BCPSs constitute a Single Instruction Multiple Data processor made of a highly interconnected mesh of 2048×6 processing elements.
- Finally, the tracks found by the BCPSs are counted and a decision is taken by the BCPC (Beauty Contiguity Processor Controller) according to the chosen triggering criteria of number of primary and number of high impact parameter tracks (three primary and two secondary were used for WA92 data taking).

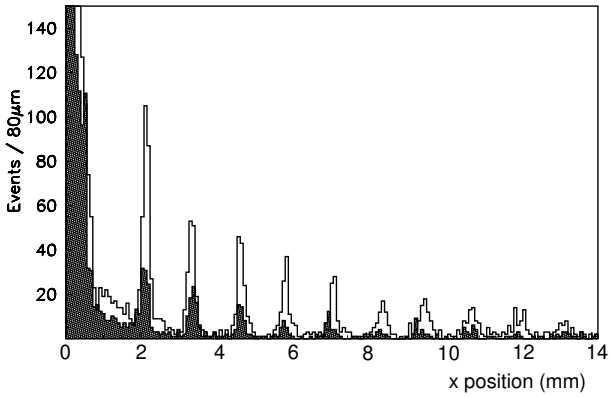

Figure 17: *Effect of the Beam Filter Processor (BFPR): (a) Distribution (unshaded) of primary vertices triggered by BCP. (b) Distribution (shaded) of primary vertices triggered by BCP·BFPR. The target centre is at $x = 0$.*

The whole system is very compact: in spite of the large number of channels (25 000) read out by the COROMs (7 Fastbus modules) and the complexity of the BCP (12 Fastbus modules), it requires only one Fastbus crate. The BCP requires 35 μs to process an event, independent of the number of tracks in the event. Although "algorithm-specific" it has considerable flexibility, in that several different definitions of the trigger topology can be selected during data taking. The performance is illustrated in Figure 18, which compares the projected impact parameter to the primary vertex of all reconstructed tracks, with and without the BCP. A trigger rate of 3.9%, relative to INT, was achieved using the 3-primary, 2-secondary algorithm (see Table 4).

7.8 The Level–2 trigger

During "wait Level-2" the BCP reads the silicon microstrip data and processes the event. Signals from the muon processor, ECAL, and high-p_T triggers are combined with the BCT to form the overall Level-2 decision. The hardware allows various trigger conditions to be selected: the combination used for the 1993 data taking is shown in Figure 11. Only the di-muon trigger is formed without the BCT coincidence. Some Level-2 dead time is saved with an abort formed from the COROM and BFPR, when the beam finding algorithm fails. Following this abort, 15 μs is allowed for the Amplex (DkD read-out) recovery. An event, satisfying any one of the trigger conditions yields GEV (Good EVent) and starts the data acquisiton, introducing a dead-time $\sim$ 1 ms.

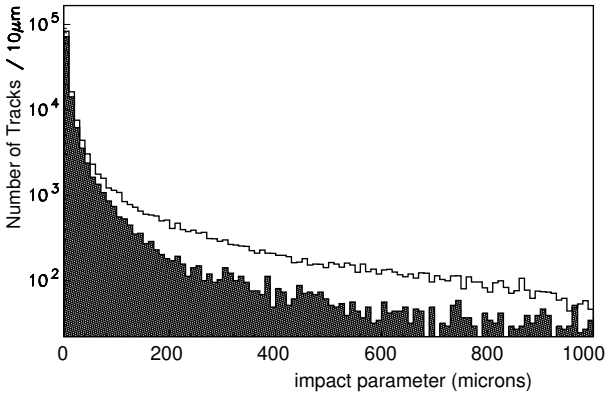

Figure 18: *Distribution of projected impact parameter of all tracks in an event to the primary vertex: the result using events triggered by INT is shown shaded, the unshaded distribution is from events triggered by INT·BCT (which have a higher average track multiplicity). The two distributions have been normalised to the same number of events.*

7.9 Trigger performance

Typical rates and dead times are displayed in Figure 11. A π^- beam rate of 1.6 MHz and a 1.03% interaction length target (2mm Cu) imply a minimum bias interaction rate of 17 kHz. The interaction trigger (INT) runs at 11 kHz producing events with an interaction in the target (and a small fraction, $\sim$ 4%, having primary vertices in the first few planes of the decay detector). The BFPR was able to reject these events efficiently (as explained in Sect. 7.7 and Ref. [8]) during "wait Level-2". The Level-1 rate was 2 kHz, a $\times 5$ reduction on the INT rate. The majority of the signal enrichment and of the rate reduction are achieved at the Level-2 trigger, which provides 300 triggers per burst. An average rejection of 98.4% of inelastic pion interactions in the target was achieved. Data were recorded between beam spills on IBM 3480 cassettes (using two tape drives). An overall experimental sensitive time close to 60% was achieved. Tagging of trigger conditions in three 16-bit words and recording of special runs allowed offline trigger analysis and verification.

8 Data Acquisition

8.1 Introduction

The WA92 data acquisition (DAQ) system is a distributed multiprocessor system implemented in the VME standard. It was designed to control the read-out from the sub-detectors and to format the data written to tape. Read-out time is reduced by incorporating four parallel streams and large buffer memories. A VAX 6310 provides the run control user interface, data recording and on-line monitoring tasks.

8.2 VME hardware architecture

Each sub-detector is read out by a Local System Crate (LSC). An LSC consists of a VME crate containing 3 basic modules [2)] and the interfaces dedicated to a particular detector. The basic modules are:

- FIC (Fast Intelligent Controller), a processor board equipped with a Motorola 68020/30.
- VIC 8250, to interconnect the VME crates via the VMV cable bus.
- CORBO, to distribute the trigger signals to the VME crate.

Data from the various detectors are read in parallel by the LSCs. The WA92 system consists of 4 LSCs, used to read data from the sub-detectors during the beam spill, and one event builder.

- LSC1: reads the Decay Detector, Omega Chambers and hodoscopes (CAMAC bus)
- LSC2: reads the OLGA fastbus ADCs
- LSC3: reads the Muon VME bus
- LSC4: reads the vertex detector COROMs.

8.3 Software Implementation

The DAQ has been implemented in an OS–9 environment. The Front-End system uses three layers of software. The lowest layer provides drivers which handle interrupts from the different devices (e.g. FICs FIFOs and the CORBO). These drivers handle only device specific aspects and call a routine installed dynamically by the next layer of software, the 'data acquisition driver' (DAQDRV). An OS–9 process forms the third layer of the system. For each trigger (Event, Start/End of Run or Spill) a user-provided subroutine is called with a pointer to a data buffer. All other functions, such as data block formatting, and compiling of acquisition data-flow statistics are performed by this OS–9 process.

The Event-building task is fully data driven and is performed outside of the beam spill. Data are arranged in buffers of 32 kbyte (super events) and transferred to the VAX 6310, which records the data on IBM 3480-compatible cassettes using two DEC TA90 cartridge drives. Each cassette has a 210 Mbyte capacity and holds approximately 25 000 WA92 events (8000 bytes/event).

8.4 Performance

On receipt of event triggers, the intrinsic dead time from software overheads is about 150 μs. Transfer of data to the LSCs is completed in about 1 ms. For an average of 300 standard trigger events per spill the DAQ introduces a dead time of the order of 20%. We achieved a transfer rate between LSC and event builder of the order of 1 Mbyte/s, and there is no limitation due to transfer rates outside of the beam-spill.

[2)] Manufactured by CES, Geneva, Switzerland

9 Off-line reconstruction

Track reconstruction in the Ω spectrometer is performed by the TRIDENT programme [11]. The use of the Decay Detector (DkD) and the Vertex Detector (VxD) and the specific needs of the WA92 experiment required several modifications and additions that are described below. We use the abbreviation "Ω-track" to mean tracks reconstructed using only the MWPC and drift chambers, and "silicon-track" to mean, reconstructed using data only from the DkD and VxD detectors. The essential steps in pattern recognition and track fitting are the following:

- Find tracks using all the tracking detectors: since we have a thin target (2 mm thickness) and a precisely measured beam ($\sigma_{y,z} \sim 5\,\mu$m), we use the position at which the extrapolated beam crosses the target median plane. A first track reconstruction is made using this constraint together with the information from the Ω MWPCs and drift chambers.
- Delete the non-interacting beam tracks in the x-z projection of the DkD. Any track candidate with 9 or more digitizings, a dip angle smaller than 3 mrad with respect to the mean beam direction and an impact parameter to the primary vertex in the range $0.2 - 5$ mm is classified as a non-interacting beam track: the corresponding hits are flagged and are not used in the following steps.
- Find the tracks in the x-z projection of the DkD and the VxD: all possible candidates with specific requirements on the minimum number of hits, on the maximum gap (defined as number of contiguous missing planes) and on the number of shared hits, are filtered by cutting on the track χ^2 and on the impact parameter (h) to the primary vertex. To reduce the number of ghost-track candidates this search is done iteratively, with varying cuts. The hits of accepted candidates are erased and are not used in the following stages. The minimum requirements to accept a track candidate are: either ≥ 4 VxD or ≥ 3 VxD and 3 DkD digitizings, a gap less than 3 planes, $h < 1.2$ mm and $\chi^2/N < 2$ (where N is the number of degrees of freedom). Sharing of hits is required to be $< 40\%$ for a track. To recover large h tracks, a final search is made requiring $\geq$3 VxD digitizings, χ^2/N< 3.6 and $h < 3$ mm.
- Find, in the bending (x-y) projection, the VxD track candidates using the same method as described in the previous step (except that a second order fit is used). In this projection the minimum requirements to accept a track candidate are: $\geq$4 VxD hits, a maximum gap of 2 planes, $h < 1.4$ mm and $\chi^2/N < 4$ and the hit sharing fraction $< 40\%$. The VxD track candidates are then extrapolated into the DkD and track segments with 2 or more hits are built from the DkD hits lying near the extrapolated track: segments whose parameters differ by less than 60 μm in distance and less than 2 mrad in angle are associated to the track candidate.
- The x-y projection has fewer constraints than the x-z projection and many ghost-tracks are generated at this stage. The problem is reduced to an acceptable level (a few percent) by combining the two projections and predicting hits in the U/W chambers of the VxD. A track-projection pair is accepted if confirmed by one or more hits in U/W, and if its angles are compatible within 1.0 mrad in dip and 1.5 mrad in azimuth with the angles of an Ω MWPC track. To recover large h tracks, the final search is done requiring $\geq$3 VxD hits, $\chi^2/N < 4.6$ and $h < 3$ mm.
- Match Ω-tracks to the silicon-track candidates: by comparing (see Fig. 19) the track parameters, curvature, angles and position at a y-z reference plane, 98% of the silicon-tracks are matched to the Ω-tracks. Only 75% of the Ω-tracks match the silicon-tracks, but this percentage increases to 85% for tracks with momentum larger than 20 GeV/c. Unmatched Ω-tracks are then extrapolated into the DkD and VxD and unmatched silicon-track candidates, or unused hits lying within a road, are added to the tracks. This last search increases the average number of tracks from 11 to 12.9 per event. (These numbers refer to the Cu target. For the W target a 10% higher multiplicity was observed.)
- Perform a global track fit using the selected hits in the Ω chambers and the silicon detectors following the method described in [11]. The full error matrix for the space points is used in the fit. It includes the measurement errors and the contribution of the multiple scattering in the DkD and VxD planes. This fit improves the accuracy on momentum measurements to $\sigma_p/p^2 = 1.6 \times 10^{-4}\,(\mathrm{GeV}/c)^{-1}$ and improves the precision on track parameters in the region where secondary vertices due to heavy-flavour decays should be found.

Figure 20 shows the impact-parameter distribution, the distance of closest approach of tracks to the primary vertex. It indicates the magnitude of track measurement errors at the vertex, compared with the mean impact parameter expected in B-decays, which is $\sim 450\,\mu$m.

The vertex reconstruction is based on an iterative method which uses the track parameters

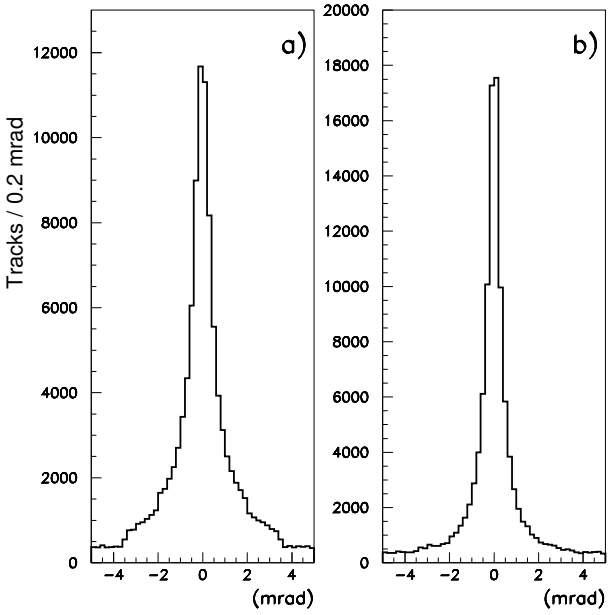

Figure 19: *Difference between: (a) the azimuth angle measured by the silicon detectors and the same quantity measured by Omega MWPC's; (b) Same for the dip angle. The FWHM values are 1.0 and 0.7 mrad respectively for the azimuth and for the dip.*

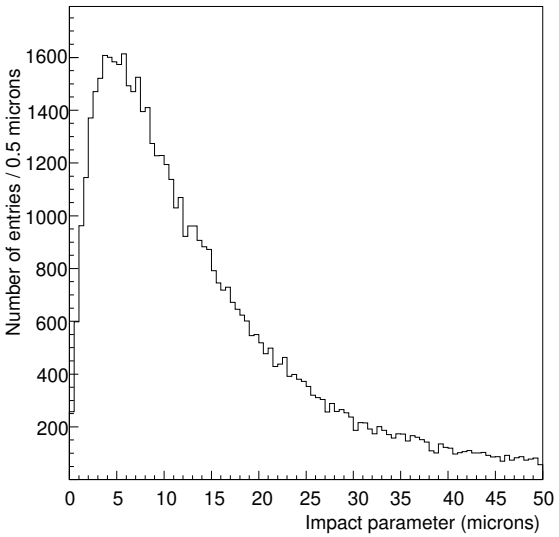

Figure 20: *Impact parameter distribution of tracks from the primary vertex.*

(and error matrix) at the first (upstream) measured point. Candidate vertices are chosen according to a strategy that assigns a large weight to the beam track (which suffers negligible multiple scattering and is precisely measured by 10 planes of 20 μm pitch silicon detectors). Spatial separation of the incoming and the outgoing tracks distinguish "primary" tracks, that intersect the beam trajectory in the target region, ($\Delta x \leq 2$ mm from the target centre), from "secondary" tracks. The two classes are kept separate and, within each class, pairs of tracks are intersected . All the intersections closer than $2\,\sigma$, that is, twice the r.m.s error on the intersection position, are merged in clusters whose tracks are filtered by a linear Kalman fitting algorithm [18] in order to evaluate the vertex positions. After this fit, tracks not belonging to any vertex undergo a "last-chance" procedure of intersection, clustering and fitting, in order to recover wrong assignments in the first choice of tracks. The mean errors on the primary vertex x-position and on those of secondary vertices are given in Table 3. The secondary vertices are classified according to the number of charged tracks and also according to whether their origin occurs in the DkD or the VxD detectors. The calculated error on the secondary vertices x-position is consistent with the measured width of the distributions of secondary interactions on the DkD planes (see Section 3.2.3).

10 Simulation

The WA92 event simulation involves four basic operations, namely event generation, tracking of particles through the experimental apparatus, event spoiling and reproduction of the various triggers.

Minimum-bias events are generated using Fluka [19] as interfaced to Geant 3.21 [20], it having been found in trials carried out with Fluka, Fritiof [21] and Gheisha [22] that Fluka, after a slight adjustment to the default p_{T}^2 spectrum, best reproduced the observed characteristics of interactions recorded in the WA92 experiment. Comparison with published data [23] indicates that the modelling of the production of heavily ionizing particles, important for the simulation of the behaviour of the in-target counter (IT), is reasonably accurate in Fluka.

Events in which there is creation of a heavy quark, Q, and its antiquark, $\bar{\mathrm{Q}}$, are generated using a combination of Pythia 5.4 [24], this providing the description of hard processes, Jetset 7.3 [25] and Fluka. Pythia, following leading-order perturbative QCD calculations, simulates the production of a $\mathrm{Q}\bar{\mathrm{Q}}$ pair in a collision between a π^- having a fraction, ξ, of the beam-pion momentum and a nucleon, where if the target nuclei have atomic number Z and nuclear mass number A the probability of the nucleon being a proton is Z/A. Use is made

	$\sigma_x(\mu m)$	$\sigma_y(\mu m)$	$\sigma_z(\mu m)$
primary vertex	115	4	3
2-prong secondary vertex (DkD)	274	11	8
3-prong secondary vertex (DkD)	210	8	6
4-prong secondary vertex (DkD)	141	6	4
2-prong secondary vertex (VxD)	424	12	11
3-prong secondary vertex (VxD)	310	9	8
4-prong secondary vertex (VxD)	234	7	6

Table 3: Precision in vertex reconstruction.

of the EHLQ [26] structure functions for nucleons and of the Owens [27] structure functions for pions. For the generation of $b\bar{b}$ events ξ is assigned a fixed value of $340/350 \approx 0.97$, whereas for the generation of $c\bar{c}$ events ξ is distributed as $P(\xi) \sim \xi^5(1-\xi)$ and has a mean value of 0.75, tuned to give agreement with experimental data. The Q and the $\bar{Q}$ fragmentation are performed by Jetset in accordance with the Lund [28] string model. Information relating to the particles produced in the fragmentation is saved and the fraction of the beam-pion momentum not carried away by these particles is calculated. Fluka then simulates an interaction between a π^- having this calculated momentum and a target nucleus. A complete event consists of the $Q\bar{Q}$ fragmentation products and the Fluka interaction products.

The tracking of particles through the experimental apparatus (Fig.21) is accomplished using Geant 3.21, with reference to a detailed map of the Omega magnetic field, and is largely standard. An incoming 350 GeV/c π^- is directed towards the target from slightly upstream of the beam hodoscope and the point at which it interacts is determined by Geant. The particles that emerge from this primary-interaction point are those given by the event generator. A user may force Geant to locate the primary interaction in the target, or else may allow the occurrence of a primary interaction anywhere between the most upstream plane of the beam hodoscope and the most downstream plane of the decay detector, events where the primary interaction takes place outside of the target contributing ~4% of all Level-2 triggers. The simulation of the apparatus comprises representations of the spectrometer magnet and of the detector supports, in which particles may interact, as well as of the detectors themselves. Long-lived decays of charged π and K mesons, and neutral strange particle decays are simulated directly through Geant. Decays of particles not described in the default Geant data tables, and including all hadrons containing b or c quarks, are defined by Jetset 7.4 [29], interfaced with Geant for this purpose. Energy depositions in the decay detector, in the IT counter and in the electromagnetic calorimeter are converted into analogue signals, with full modelling of charge-carrier diffusion in the case of the decay detector and with energy-attenuation effects taken into account in the case of the calorimeter. Energy depositions in the other detectors of the experiment, including muon tracking and hadron showers in the iron filter, are converted into binary signals.

In the course of the event spoiling, out-of-time beam particles, detector inefficiencies and random noise are added in accordance with measurements from real data. As in the experimental situation, the out-of-time beam particles and, where relevant, their interaction products are registered only by the decay detector and, with a ~20% lower probability, by the beam hodoscope and by the vertex detector.

The steps followed by the online processors in arriving at the trigger decisions are closely mimicked in the simulation. Most notably, a BCP simulator, which is written partly in VAX11 macro-assembler and obeys exactly the instruction set used to program the BCP hardware, has been developed [7]. The range of trigger rates for the Cu target, experimentally observed over the data taking period, and the rates obtained from a consideration of simulated minimum-bias events are compared in Table 4. The output for a fully simulated event is a ZEBRA [30] structure that includes the event kinematics, the trigger responses, a record of the signals from the detectors and details of the associations between these signals and the generated particles. These data may be used in simulation-specific studies, for example when optimising vertex-reconstruction algorithms, or may be

	Experiment	Simulation
INT/$\sigma_{\text{inelastic}}$	60-65%	62.1±0.7%
$\geq 1\mu$/INT	2.9%	2.8±0.1%
$\geq 2\mu$/INT	0.09%	0.06±0.01%
$\geq 1p_T$/INT	41%	40.7±0.4%
$\geq 2p_T$/INT	12.7%	10.4±0.2%
$\geq 2E_T$/INT	2.6%	2.6±0.1%
BCP(3,1)/INT	14%	15.8±0.2%
BCP(3,2)/INT	3.9%	3.5±0.1%

Table 4: *Comparison between inclusive trigger rates observed experimentally with the Cu target and the corresponding rates given by the simulation for minimum-bias events (dead-time effects excluded).*

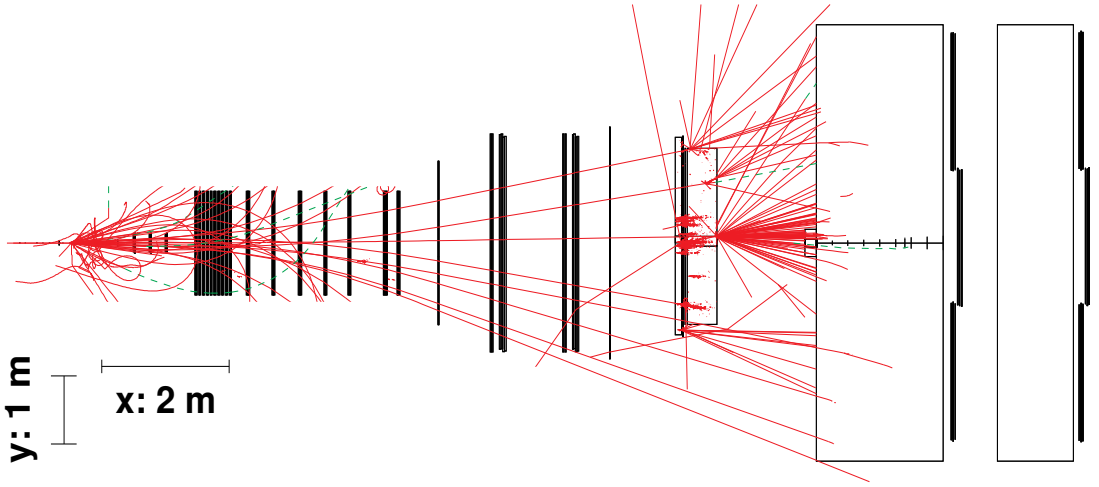

Figure 21: *Charged-particle tracks traced by Geant (x-y projection) in a simulated interaction.*

analysed in the same way as the experimental data.

Evidence that the simulation accurately describes the experimental situation is provided by a comparison of results obtained from the Trident reconstruction of simulated minimum-bias events selected by the interaction trigger with the corresponding results for experimental data recorded with this trigger (Figures 22-24). In particular, the simulation reproduces the distributions of primary-vertex x-coordinates before and after the request for a signal from the IT counter (Figure 22), the primary and non-primary track multiplicities (Figure 23) and the track kinematics (Figure 24).

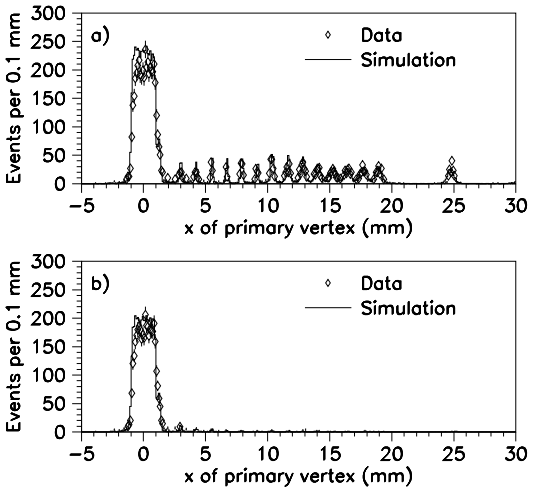

Figure 22: *Comparison between simulation and experiment of primary-vertex position, reconstructed by Trident, for triggered interactions: a) when the response of the IT counter is not considered and b) when it is required that the IT counter records a signal. Event samples are normalised to the same number of triggered interactions.*

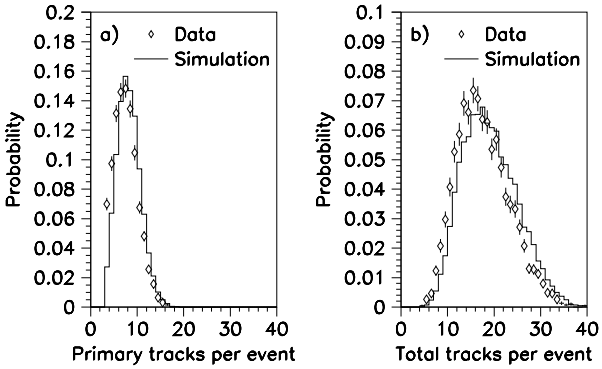

Figure 23: *Comparison between simulation and experiment of a) primary-track multiplicity and b) total track multiplicity as given by Trident for events selected with interaction trigger.*

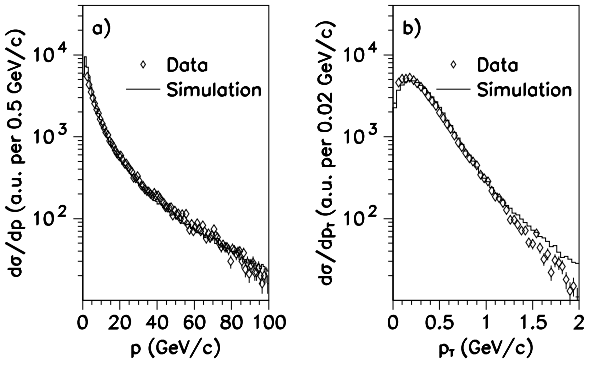

Figure 24: *Comparison between simulation and experiment of a) momentum distribution and b) transverse-momentum distribution for tracks reconstructed by Trident in the case of events selected by the interaction trigger. Event samples are normalised to the same number of tracks.*

11 Overall Performance

The experimental luminosity was calculated from

$$\mathcal{L} = \frac{N_{\mathrm{INT}}}{\varepsilon \cdot \sigma_{\mathrm{inel}}} ,$$

with N_{INT}, the number of INT triggers producing primary vertices in the target, ε the INT trigger acceptance (estimated from the simulation) and σ_{inel} the inelastic cross-section for the target material. During data taking in 1992 and 1993, a total of 7×10^9 π^- interactions in the Cu and in the W targets resulted in the experimental luminosities listed in Table 5. The Level-2 trigger retained 2% of these interactions. The precision on the numbers is $\pm 6\%$, limited by the ability to simulate the effect of the IT counter threshold and by the precision in measurements of the inelastic cross-sections.

The numbers of events, of any particular type, written to tape are given by the product of the luminosity, the cross-section and the corresponding trigger acceptances, which are obtained from the Monte Carlo simulation. The acceptances of various components of the trigger, for generic decays of b and of c-hadrons, are listed in Table 6. The INT acceptance is relative to all inelastic interactions, other figures are relative to INT.

To illustrate the overall performance of the trigger selection and of the event reconstruction precision, we present experimental data on invariant-mass distributions. In Figure 25 the D-meson peak ($19\,\mathrm{MeV}/c^2$ FWHM) is clearly resolved from background. The lower histogram results following cuts on the pulse-height of the DkD signals, as described in section 3.2.4. The background under the signal peak is halved while the loss of signal is 8%.

Figure 26 shows the distribution of the invariant mass of muon pairs where the peaks coming from the $\mu^+\mu^-$ decays of neutral vector mesons are clearly visible above a background from in-flight decays of pions and kaons. The J/ψ mass is reconstructed with a precision (FWHM) of $30\,\mathrm{MeV}/c^2$, a significant contribution to which is Coulomb scattering in the target.

All these distributions are well reproduced by Monte Carlo generated events with full simulation of the detector response.

12 Conclusions

The signal-to-background ratio for production of heavy-flavoured hadrons in fixed-target experiments is very low, especially for b-hadrons. The WA92 experiment employed specific triggers and detectors to meet this challenge. An impact parameter trigger, using hits from silicon microstrip detectors, combined with muon and high-p_{T} trigger enriched the heavy-flavour content of the recorded events. For b-hadron decays the enrichment factor achieved was 14. The use of a high-precision decay

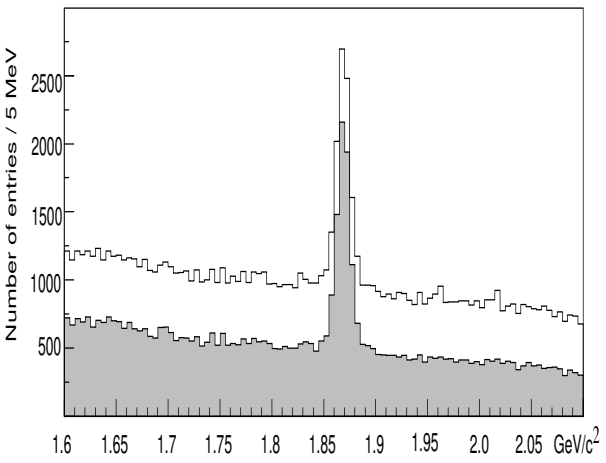

Figure 25: *Invariant mass distribution showing D-decays in* K$n\pi$ *combinations. The shaded histogram contains the same data sample but with a pulse height cut applied to the signals from the decay detector.*

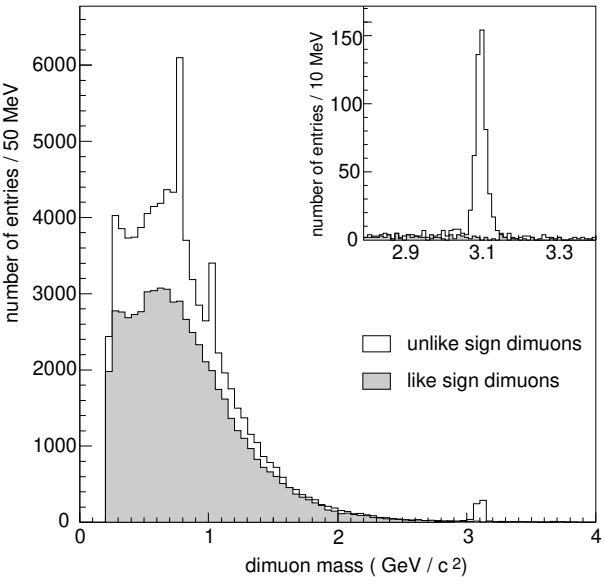

Figure 26: *Invariant mass distributions for muon pairs. The inset shows a magnified display of the* J/ψ *mass region.*

	Cu 1992	W 1992	Cu 1993
Luminosity (events nb^{-1})	2.8	1.5	5.3

Table 5: *Experimental Luminosities*

Trigger	INT	BCT	μ	2μ	p_T	Level-2
Acceptance for Beauty	0.71	0.40	0.19	0.02	0.64	0.33
Acceptance for Charm	0.81	0.13	0.077	0.0028	0.48	0.11

Table 6: *Trigger acceptances for b and c-hadron decays*

detector permitted identification of the event topology in the region where decays of heavy-flavoured hadrons occur. The precision in vertex reconstruction corresponded to 3.7% of the mean B-decay proper lifetime. Analogue charge signals from the silicon detectors provided a powerful tool to distinguish decay vertices from backgrounds due to interactions in the silicon planes.

An analysis of the data taken with the copper target in 1992 was undertaken and a preliminary measurement of the B-production cross-section has been published [31].

Acknowledgements

The construction and operation of the experiment would have been impossible without the skill and assistance of a motivated technical team. We thank, in particular; F.Bronzini, S.Di Marco, E.Gennari, M.Perciballi and A.Tusi for the RPC mechanics, read-out electronics and trigger processor; R.Cereseto, A.Corre, C.Pizzorno, L.Cracco and C.Veccia for the preparation of the mechanics and the read-out of the vertex detector; E.Chesi, F.Cossey, A.Menetrey and R.Pegaitaz for the assembly and tests of the silicon decay detector. The assistance from P.Grafstrom in tuning the beam, from R.Sené in setting up the bow-tie hodoscopes and V.Cecconi for data handling is gratefully acknowledged.

We acknowledge the financial support received from our national funding authorities, INFN, Italy and SERC, UK. Those of us from non-member states thank CERN for its hospitality.

References

[1] W. Beusch et al.,
CERN/SPSC 77/70 (1987).

[2] M.Adinolfi et al.,
Nucl. Instr. and Meth., A329 (1993) 117.

[3] E.H.M. Heijne and P. Jarron,
"A Low Noise CMOS Integrated Signal Processor for Multielement Particle Detectors",
preprint CERN/EF-88-5, April 1988.

[4] E.Chesi and P.Martinengo,
"Digital Readout for Analog Multiplexed Signals (DRAMS), CERN experiment PS202 internal note, September 1988.

[5] A. Beer et al.,
Nucl. Instr. and Meth. A337 (1994) 280.

[6] G. Darbo and L. Rossi,
Nucl. Instr. and Meth. A289 (1990) 584.

[7] C. Bruschini,
"Studio di un Trigger rapido su vertici secondari per la ricerca di particelle dotate di Beauty", Thesis, University of Genova, 1994.

[8] G. Darbo,
Nucl. Instr. and Meth A351 (1994) 225.

[9] J.Batten et al.,
Nucl.Physics B (Proc.Suppl) 44 (1995) 435.

[10] G. Darbo and S. Vitale,
Nucl. Instr. and Meth. 190 (1981) 81.

[11] J. C. Lassalle et al.,
Nucl. Instr. and Meth. 176 (1980) 371.

[12] A. Beer et al.,
CERN Yellow Report 78-14 (1978)

[13] P.Astbury et al.,
Physics Letters 152B (1985) 419.

[14] W. Beusch et al.,
Nucl. Instr. and Meth. A249 (1986) 391.

[15] E. Petrolo and S. Veneziano:
Nucl. Instr. and Meth. A315 (1992) 95.
E. Gennari, E. Petrolo and S. Veneziano:
IEEE Trans. on Nucl. Sci. NS-39 (1992) 821.

[16] C. Bacci et. al.:
Nucl. Instr. and Meth. A324 (1993) 83.

[17] R. Cardarelli and R. Santonico:
Nucl. Instr. and Meth. 187 (1981) 377.
A. Di Biagio et. al.:
Nucl. Instr. and Meth. A263 (1988) 20.

[18] P.Billoir,
Nucl. Instr. and Meth. A241 (1985) 115.

[19] A. Fassò et al.:
Proc. IV Int. Conf. on Calorimeters and their Applications, World Scientific, (1994) 493.
[20] GEANT Detector Description and Simulation Tool, CERN Program Library Long Writeup W5013 (1994).
[21] H. Pi,
Comput. Phys. Commun. 71 (1992) 173.
[22] H.C. Fesefeldt, RWTH Aachen Physikzentrum report PITHA 85-02 (1985).
H. Fesefeldt,
Nucl. Instr. and Meth. A292 (1990) 279.
[23] S. Fredriksson et al.,
Phys. Rep. 144 (1987) 187.
[24] T. Sjöstrand and M. Bengtsson,
Comput. Phys. Commun. 46 (1987) 43.
[25] T. Sjöstrand and M. Bengtsson,
Comput. Phys. Commun. 43 (1987) 367.
[26] E. Eichten et al.,
Rev. Mod. Phys. 56 (1984) 579.
E. Eichten et al.,
Rev. Mod. Phys. 58 (1985) 1065.
[27] J.F. Owens,
Phys. Rev. D30 (1984) 943.
[28] B. Andersson et al.,
Phys. Rep. 97 (1983) 31.
[29] T. Sjöstrand,
Comput. Phys. Commun. 82 (1994) 74.
[30] The ZEBRA system, CERN Program Library Long Writeup Q100/Q101 (1993).
[31] L.Rossi et al.,
Proc. XXVII Int. Conf. on High Energy Physics, Glasgow,UK, 20-27 July 1994, p.1027.